O₃-precursor relationship over multiple patterns of time scale:

A case study in Zibo, Shandong Province, China

Zhensen Zheng[1], Kangwei Li[2,3*], Bo Xu[4], Jianping Dou[5], Liming Li[1], Guotao Zhang[1], Shijie Li[1], Chunmei Geng[1], Wen Yang[1], Merched Azzi[6], Zhipeng Bai[1*]

[1] State Key Laboratory of Environmental Criteria and Risk Assessment, Chinese Research Academy of Environmental Sciences, Beijing 100012, China
[2] Univ Lyon, Université Claude Bernard Lyon 1, CNRS, IRCELYON, F-69626 Villeurbanne, France
[3] Department of Environmental Sciences, University of Basel, 4056, Basel, Switzerland
[4] Zibo Eco-Environmental Monitoring Center, Zibo 255000, China
[5] Zibo Ecological Environment Quality Control Service Center, Zibo 255095, China
[6] New South Wales Department of Planning, Industry and Environment, PO Box 29, Lidcombe, NSW 1825, Australia

*Corresponding authors:
Kangwei Li (likangweizju@foxmail.com, kangwei.li@unibas.ch) and Zhipeng Bai (baizp@craes.org.cn)

Abstract. In this study, we developed an approach that integrated multiple patterns of time scale for box modeling (MCMv3.3.1) to better understand the O₃-precursor relationship through multiple sites and continuous observations. A five-month field campaign was conducted in the summer of 2019 to investigate the ozone formation chemistry at three sites in a major prefecture-level city (Zibo) in Shandong province of northern China. It was found that the relative incremental reactivity (RIR) of major precursor groups (e.g., anthropogenic volatile organic compound (AVOC), NO$_x$) was overall consistent in the sign along with time scales changed from wider to narrower (four patterns: five-month, monthly, weekly, and daily) at each site, though the magnitudes of RIR varied at different sites. The time series of the photochemical regime (using RIR$_{NOx}$/RIR$_{AVOC}$ as indicator) in weekly or daily patterns further showed a synchronous temporal trend among the three sites, while the magnitude of RIR$_{NOx}$/RIR$_{AVOC}$ was site-to-site dependent. The derived RIR ranking (top 10) of individual AVOC species showed consistency at three patterns (i.e., five-month, monthly, and weekly). It was further found that the campaign-averaging photochemical regimes showed overall consistency in the sign but non-negligible variability among

38   the four patterns of time scale, which was mainly due to the embedded uncertainty in
39   model input dataset when averaging individual daily pattern into different timescales.
40   This implies that utilizing narrower time scale (i.e., daily pattern) is useful to derive
41   reliable and robust O_3-precursor relationship. Our results highlight the importance of
42   quantifying the impact of different time scales to constrain the photochemical regime,
43   which can formulate more accurate policy-relevant guidance for O_3 pollution control.
44

1 Introduction

46   Since 2013, the ambient $PM_{2.5}$ concentration in China has dramatically declined
47   by implementing Clean Air Action (Lu et al., 2018; Wang et al., 2020b; Zhang et al.,
48   2019). However, national ground surface ozone concentrations increased over the same
49   period (Xue et al., 2020) and became a major air quality problem that needed to be
50   addressed in China (Li et al., 2019; Wang et al., 2019). It is well-known that ground
51   surface ozone is formed mainly by complex nonlinear photochemical oxidation of
52   volatile organic compounds (VOCs) in the presence of nitrogen oxides ($NO_x = NO +$
53   NO_2) and sunlight (Blanchard, 2000; Hidy, 2000; Kleinman, 2000), which adversely
54   influences human health, vegetation and corps (Brunekreef and Holgate, 2002;
55   Vingarzan, 2004).
56   Given the complex non-linear relationship between O_3 formation and its
57   precursors (VOCs and NO_x), challenges in mitigating its severity lie primarily in
58   comprehensively understanding of O_3-precursor relationship (Su et al., 2018a; Tan et
59   al., 2018a). It is commonly recognized that regional-scale air quality models and the 0-
60   D box model are two mainstream approaches to investigate the increasingly severe
61   ozone problem (Blanchard, 2000; Cardelino and Chameides, 1995; Hidy, 2000; Liu et
62   al., 2019). Unlike the complicated 3-D air quality models, the 0-D box model is an
63   observation-based model that implemented with gas-phase chemical mechanism, and
64   has been widely used to diagnose O_3-precursor relationship in various locations (Liu et
65   al., 2021a; Sun et al., 2016; Tan et al., 2019b; Xue et al., 2014a; Yu et al., 2020a). Some
66   previous studies (Li et al., 2021; Lu et al., 2010a; Sicard et al., 2020; Yu et al., 2020b)
67   have reported a large variability of O_3-precursor relationship in spatiotemporal scales
68   in many cities of China, which indicates great challenges in current O_3 pollution control
69   (Wang et al., 2017a; Xue et al., 2014b).
70   **Table 1** summarizes the published studies of O_3-precursor relationship using the
71   0-D box model (implemented with different gas-phase chemical mechanisms) at
72   diversified patterns of time scale in many places of China. The observational period in
73   most previous studies was short-term (i.e., less than one month), while medium-term
74   (i.e., from one to several months), and long-term (i.e., multiple years) periods were
75   limited. As shown in **Table 1**, we find that model input datasets with different

76 timescales have been employed in previous studies to identify the campaign-averaging
77 O_3 formation regime, but there is a lack of comparison among these different timescales.
78 We also find that more than half of the studies using the averaged diurnal patterns as
79 box model input, which is particularly common for those medium and long-term
80 measurements. For example, a 10 years long-term observational study by Wang et al.,
81 (2017a) adopted monthly pattern of time scale for model simulation with the reason of
82 saving computing resources, and it also revealed a substantial temporal variability of
83 O_3-precursor relationship. In addition, it is believed that long-term (measurements of at
84 least several months) and multiple-site continuous online measurements can provide
85 opportunity to develop O_3 control strategy more comprehensively over a wider
86 spatiotemporal scale (Li et al., 2021; Wang et al., 2017b; Wang et al., 2017b). However,
87 such measurements have been quite rare in China, limiting the present understanding
88 of O_3-precursor relationship (Lu et al., 2019; Wang et al., 2017b).

89   In this study, a five-month field campaign was conducted in the summer of 2019
90 to investigate the ozone formation chemistry at 3 sites in Zibo, a major prefecture-level
91 Chinese city in Shandong province. According to our measurements at the three sites in
92 Zibo, the averaged O_3 concentration during the whole observational period was around
93 50 ppbv, while the daily maximum of O_3 concentrations for some extremely polluted
94 periods were nearly 120-150 ppbv (see details in **Section 3.1**). Here we developed an
95 approach that integrated multiple patterns of time scale for box model simulation, which
96 aimed at illustrating the non-linearity of O_3-precursor relationship driven by its actual
97 daily / weekly / monthly variability. Our results can be conducive to interpreting
98 variations of O_3-precursor relationship over a wider spatiotemporal scale, and they
99 provide implications for developing more precise and constrained O_3 control strategies
100 in other regions.

101 **2 Methods**

102 **2.1 Study sites and measurements**

103   Field measurements were conducted in a major prefecture-level city (Zibo), which
104 is in the middle of Shandong Province, northern China, from 1 May to 30 September,
105 2019. **Figure S1** shows the surrounding environment and geographical locations at the
106 three sampling sites; a detailed description of the Tianzhen (TZ), Beijiao (BJ) and
107 Xindian (XD) sites can be found in our previous study (Li et al., 2021). Briefly, TZ
108 contains a mixture of crude oil processing and operation stations and farming areas, and
109 is classified as suburban area; XD contains a mixture of residential and heavy industrial
110 zones, and is considered as a suburban area; BJ is in the urban area of Zibo.

111   Typical inorganic gases of O_3, NO, NO_2, CO and SO_2 were measured using online
112 commercial gas analysers (Thermo Scientific 49i, 42i, 48i and 43i, USA) at the three
113 sites. Following the Chinese meteorological monitoring regulation (GB/T 35221-2017),

114 we continuously monitored the meteorological parameters (i.e., temperature, relative
115 humidity, UV-A solar radiation, precipitation, wind speed, and wind direction) at the
116 three sites (Li et al., 2021). Two online GC systems (gas chromatography–flame
117 ionisation detector, GC-FID, Thermo Scientific GC5900) were deployed at TZ and BJ
118 respectively to measure VOC species. For C_2-C_5 VOCs, desorption and separation were
119 performed using a GC with pre-concentration on a combination of two columns,
120 followed by a FID detector. For C_6-C_{12} VOCs, air sample was pre-concentrated on
121 Tenax GR cartridges and subsequently separated by chromatographic column, then
122 detected by another FID detector. Similarly, one online system (gas chromatography–
123 flame ionisation detector/photoionisation detector, GC-FID/PID, Syntech Spectras GC
124 955-615/815) was deployed at XD site. For C_2-C_6 VOCs, the hydrocarbons were
125 concentrated on a Tenax GR carrier, then thermally desorbed and separated on a DB-1
126 column, and finally detected by FID and PID detectors. For C_6-C_{12} VOCs, the air
127 sample was concentrated on a Carbosieves SIII carrier at 5°C, then thermally desorbed
128 and separated on a combination of two columns, and FID and PID detectors were
129 employed for subsequent detection. These systems measured 55 VOC species at a 1-h
130 resolution, and more detailed descriptions can be found elsewhere (Chien, 2007; Jiang
131 et al., 2018; Xie et al., 2008).

132 **Table S1** summarized the limit of detection, accuracy, precision of the instruments
133 at the three sites, and all the measurement instruments were regularly subjected to the
134 service of checking and maintenance during the whole campaign. Unfortunately, we did
135 not conduct the inter-comparison between the GC-FID and GC-FID/PID instruments at
136 the same site due to practical reasons, as these VOC instruments were separately
137 deployed at the three different sites for continuous routine operation. To ensure the
138 quality assurance / quantity control (QA/QC) of online VOC measurement, two five-
139 point calibrations (i.e., 2, 4, 6, 8, 10 ppbv, dilution from one cylinder) for standard gases
140 with 55 VOC species (Linde Co., Ltd, USA) were carried out in May and August of
141 2019 at the three sites. **Table S2** showed that the calibration linearity (R^2) of all
142 measured VOCs were nearly 0.9990. Additionally, a single-point calibration (i.e., 6
143 ppbv) was regularly performed every month during the whole campaign. As shown in
144 **Figure S2** (a case from TZ), the retention time, peak fitting and baseline of the
145 chromatogram were manually checked and adjusted on a daily basis.

146 2.2 0-D box model and design of four patterns of time scale

147 The 0-D box model integrated with the latest Master Chemical Mechanism of
148 MCMv3.3.1 (http://mcm.york.ac.uk; last access: 27 January 2023) has been widely
149 utilized in many regions (He et al., 2019; Jenkin et al., 2015; Liu et al., 2019; Whalley
150 et al., 2021). Unlike the lumped chemical mechanisms such as CB05 (Wang et al.,
151 2017a; Yarwood et al., 2005), CB6 (Yarwood et al., 2010), RACM/RACM2 (Goliff et

al., 2013; Stockwell et al., 1997, 2020) and SAPRC-07 (Carter, 2010), the MCMv3.3.1 is a near-explicit chemical mechanism consisting of over 5,800 species and 17,000 reactions (Jenkin et al., 2015; Saunders et al., 2003), which can be used to describe the gas-phase chemistry (i.e., in-situ photochemistry). In this study, the box model (based on the Framework for 0-D Atmospheric Modeling, F0AM) (Wolfe et al., 2016) was applied and constrained by the mean diurnal profiles of meteorological data (i.e., temperature, relative humidity, and photolysis rates), 4 inorganic gases (i.e., SO_2, CO, NO, and NO_2), and 45 speciated VOCs (in MCMv3.3.1 species list; see **Table S3**). Since measured photolysis rates (J values) were not available, the measured UV-A solar radiation was used to scale the photolysis rates calculated from the Tropospheric Ultraviolet and Visible Radiation model (TUVv5.2; https://www.acom.ucar.edu/Models/TUV/Interactive_TUV; last access: 27 January 2023) following the approach of recent studies (Lyu et al., 2019; Lyu et al., 2016). Specifically, the geographical coordinates, date and time were initialized into the TUV model to derive photolysis rates and solar radiation. We obtained the scaling factor by comparing the observed with modeled solar radiation, and used this scaling factor to scale the TUV model derived photolysis rates. A dilution rate of $3/86400 \text{ s}^{-1}$ was applied for all non-constraint species and simulation days through a stepwise sensitivity test by adjusting it from $1/86400 \text{ s}^{-1}$ to $5/86400 \text{ s}^{-1}$ (see details in **Text S1**) for the best reproduction of O_3. For each model run (i.e., each daily model simulation), it was performed on a daily basis with intervals of 24 hours spanning from 0:00 to 23:00, and each individual model simulation was run to reach one-day diurnal steady state. The detailed descriptions of box model operation were provided in our previous study (Li et al., 2021).

Since the box model simulations are conducted with intervals of 24 hours spanning from 0:00 to 23:00 local standard time (Wang et al., 2018), the entire campaign observations were taken into four patterns of time scale (i.e., five-month, monthly, weekly, and daily) as diurnal average format for model input (**Figure 1**). Note that some days or weeks were not modeled due to some missing data in the measurements. Nevertheless, the total simulation number at the daily (i.e., 100, 81, and 114 days for TZ, BJ and XD respectively) or weekly (i.e., 21, 20, and 19 weeks for TZ, BJ, and XD respectively) scale was representative of the five-month campaign. Specifically, the entire campaign data classified as four patterns of time scale were modeled as base runs. Then we performed the sensitivity modeling to calculate the relative incremental reactivity (RIR) of precursors by adjusting the input concentrations in the base runs (see next section) (Lu et al., 2010a).

2.3 Calculation of net O_x production rate $P(O_x)$ and Relative incremental reactivity (RIR)

Considering the rapid chemical titration of NO to NO_2 in the presence of O_3, the concept of 'total oxidant' ($O_x = O_3 + NO_2$) has been widely used to represent the actual photochemical production of O_3 (Lu et al., 2010). Similar to those described in previous studies using the 0-D box model (He et al., 2019; Lyu et al., 2016), the net or in-situ O_x production rate ($P(O_x)$) is defined as the difference between the O_x gross production rate ($G(O_x)$) and the O_x destruction rate ($D(O_x)$), which is formulated in accordance with Eq. (1):

$$P(O_x) = G(O_x) - D(O_x) \tag{1}$$

The O_x gross production rate ($G(O_x)$), or the total chemical production of O_x, is calculated by summing the rates of oxidation of NO by HO_2 and RO_2 radicals in accordance with Eq. (2):

$$G(O_x) = k_{HO_2+NO}[HO_2][NO] + \sum k_{RO_{2,i}+NO}[RO_{2,i}][NO] \tag{2}$$

The O_x destruction rate ($D(O_x)$), or total chemical loss of O_x, is calculated by summing O_3 photolysis, the reaction of O_3 with OH, HO_2 and alkenes, as well as the reaction between NO_2 and OH, as described by Eq. (3):

$$D(O_x) = k_{O^1D+H_2O}[O^1D][H_2O] + k_{OH+O_3}[OH][O_3] + k_{HO_2+O_3}[HO_2][O_3] + k_{alkenes+O_3}[alkenes][O_3] + k_{OH+NO_2}[OH][NO_2] \tag{3}$$

Concentrations of radicals and intermediates are obtained from the outputs of the 0-D box model. The k values in Eq. (2) and (3) represent the rate constants of the corresponding reactions, respectively. The subscript 'i' in Eq. (2) represents the individual RO_2 species.

Additionally, relative incremental reactivity (RIR) has been widely used as a metric to quantify the O_3-precursor relationship, and it can be derived from the 0-D box model (MCMv3.3.1) by changing the input mixing ratios of its precursors (Sillman, 2010; Xue et al., 2014a). The RIR is defined as the ratio of percentage change in net O_x ($O_x = O_3 + NO_2$) production rate $P(O_x)$ (Li et al., 2021) to percentage change of concentration of precursor X. The RIR of a specific precursor X is described in Eq. (4):

$$RIR(X) = \frac{[PO_x(CX) - PO_x(CX-\Delta CX)]/PO_x(CX)}{\Delta CX/CX} \tag{4}$$

Here, X is a specific precursor (i.e., NO_x, CO or grouped / individual VOC species), CX is the measured concentration of precursor X, and ΔCX is the hypothetical concentration change ($\Delta CX/CX = 10\%$ in this study in accordance with the previous studies (Lyu et al., 2016; Wang et al., 2018)). $PO_x(CX)$ represents the simulated O_x production rate in a base run, whereas $PO_x(CX-\Delta CX)$ is the simulated O_x production in a second run with a hypothetical concentration change of species X. Obviously, a higher positive value of RIR(X) suggests a more effective way of reducing the ambient

225   O_3 production rate by reducing X (Ling et al., 2011; Zhang et al., 2008a).

226   In this study, the O_3 precursors were divided into four major categories, including

227   anthropogenic VOC (AVOC), biogenic VOC (BVOC, only isoprene in this study), CO

228   and NO_x (Tan et al., 2019b). AVOC was further divided into three subcategories: alkanes,

229   aromatics and alkenes* (the asterisk denotes anthropogenic alkenes, excluding isoprene

230   in this study) (Yu et al., 2020a). As mentioned, RIR method was applied mainly to

231   evaluate the O_3-NO_x-VOC sensitivity and determine the photochemical regimes among

232   four patterns of time scale. Thus, we calculated the RIR values of major precursor

233   groups (i.e., AVOC, BVOC, CO, NO_x, alkanes, alkenes* and aromatics) to further

234   quantify the O_3-precursor relationship.

235   In general, O_3 formation chemistry is usually classified into three regimes (i.e.,

236   VOC-limited, transitional and NO_x-limited) (He et al., 2019; Wang et al., 2018). In this

237   study, RIR_{NOx}/RIR_{AVOC} (the ratio of two RIR values) was used as a metric to classify

238   the photochemical regimes (Li et al., 2021). Specifically, RIR_{NOx}/RIR_{AVOC} value of less

239   than 0.5 was defined as VOC-limited regime, greater than 2 as NO_x-limited regime, and

240   from 0.5 to 2 as transitional regime (see **Text S2** and **Table S4**) (Li et al., 2021).

3 Results and discussion

3.1 Overview of the field campaign

243   **Figure 2** shows the time series of measured meteorological parameters and O_3 as

244   well as its precursors at the three sites during the whole campaign. In general, the

245   temperature (T) and relative humidity (RH) were basically consistent at the three sites,

246   while the wind speeds were different, which suggests that the three sites had an overall

247   consistent meteorological condition. In addition, the time series of UV-A radiation was

248   shown in **Figure 2d**, which was only available from one urban site of Zibo but expected

249   to represent the whole Zibo city in this study. Following the protocol of the previous

250   studies (Lyu et al., 2019; Wang et al., 2017b; Xue et al., 2014), the time series of

251   photolysis rates (e.g., J_{NO2} (**Figure 2e**) and J_{O^1D} (**Figure 2f**)) were calculated from

252   TUVv5.2 model and further scaled from UV-A radiation measurement.

253   As shown in **Figure 2g**, we found that severe O_3 pollution was observed at the

254   three sites throughout the whole campaign. According to our measurements at the three

255   sites in Zibo, the averaged O_3 concentration during the whole observational period was

256   around 50 ppbv, while the daily maximum of O_3 concentrations for some extremely

257   polluted periods were nearly 120-150 ppbv (**Figure 2g**). Interestingly, the O_3

258   concentrations at the three sites were generally consistent, while the levels of its

259   precursors (e.g., VOC, NO_x) were obviously different (**Figure 2h-k**), which implies the

260   site-to-site variation of O_3 formation chemistry for the whole Zibo city.

261   Generally, OH reactivity (or OH loss rate, k_{OH}) is widely applied to quantify the

262   capacity of OH consumption by VOCs (Tan et al., 2019a). According to **Table S3**, the

263   BVOC reactivity (k_{BVOC}, 3.5 ± 4.1 s^{-1}) in TZ were highest among the three sites. As BJ

264   was mainly influenced by the emission from urban region, it showed the highest AVOC

265   reactivity (k_{AVOC}, 6.8 ± 6.3 s^{-1}) and NO$_x$ level (31.1 ± 28.6 ppbv). In addition, XD

266   showed the highest level of alkenes* reactivity of 4.0 ± 3.2 s^{-1} within the three sites,

267   and the local petrochemical industry nearby XD area may explain such characteristic

268   (Li et al., 2021).

3.2 Evaluation of box model performance

270   The measured O$_3$ concentrations were not constrained in our MCMv3.3.1 box

271   model calculation, thus the model performance could be quantitatively assessed by

272   comparing the modeled O$_3$ (from base runs) with the measured O$_3$. **Figure S3-S8** show

273   the time series of simulated and observed O$_3$ concentrations at four patterns of time

274   scale. In most cases, the box model simulation could accurately capture the level and

275   variation trend of the observed O$_3$. However, on some days the modeling results

276   underestimated or overestimated the O$_3$ concentrations, particularly the

277   underestimation of nocturnal O$_3$ concentrations. Such discrepancies between the

278   simulated and observed O$_3$ were likely due to limitations in explicit representations of

279   atmospheric and transport processes (i.e., the horizontal and vertical transport process

280   of ground ozone) by 0-D modeling approach (Lyu et al., 2019; Yu et al., 2020b).

281   Specifically, ozone simulated by the 0-D box model is considered as in-situ

282   photochemical processes from its precursors. Unlike the 3-D air quality model, 0-D box

283   model usually simplifies the representation of the physical processes (i.e., deposition

284   and advection) (Lu et al., 2010a; Sillman, 2010). Note that some adjustable parameters

285   (e.g., radiation scheme, dilution rate) were remained consistent in all of our model

286   calculations, which ensured the comparability of model results to the greatest extent.

287   The index of agreement (*IOA*) (Li et al., 2021; Lyu et al., 2016), Pearson's

288   correlation coefficient (*r*) and root mean square error (*RMSE*) were jointly used as

289   statistical metrics to quantify the goodness-of-fit between the simulated and observed

290   O$_3$ concentrations. **Table S5** summarizes these statistical metrics for each site at various

291   patterns of time scale. Because any single statistical metric has its own limitations,

292   using these three indicators conjointly provided a more comprehensive evaluation of

293   the model performance (Su et al., 2018b). Generally, higher *IOA* and *r* as well as lower

294   *RMSE* indicate better agreement between the simulated and observed values (Wang et

295   al., 2018; Willmott, 1982). As shown in **Table S5**, slightly reduced correlation was

296   observed as the time scale changed from the wider (i.e., five-month scale) to the

297   narrower (i.e., daily scale) pattern, which is understandable because of the enlarged

298   statistical samples in the narrower pattern of time scale.

299   In summary, TZ showed the best performance of the box model simulation,

300   followed by XD and BJ, regardless of any statistical metrics or different patterns of time

scale, which may be associated with the optimized dilution rate for non-constraint species in model configuration. The overall model performance in this study (i.e., a day-to-day IOA of approximately 0.90 for TZ) was close to or slightly better than those reported in previous studies, such as $IOA = 0.74$ in Hong Kong (Liu et al., 2019), $IOA = 0.74$ in Wuhan (Lyu et al., 2016) and $IOA = 0.90$ in Jiangmen (He et al., 2019). According to the above evaluation of base runs, our modeled results were acceptable for the subsequent O_3-precursor relationship analysis described in the following sections.

3.3 Month-to-month

Figure 3a-b presents the monthly RIR values of the major precursor groups at each site, and the large variability of O_3-precursor relationship at spatiotemporal scale (i.e., site-to-site and month-to-month) was observed. Specifically, in most months, XD generally showed the highest RIR_{AVOC} among the three sites, followed by BJ and TZ. In addition, RIR_{BVOC} showed similar level to RIR_{AVOC} in TZ, but much less than RIR_{AVOC} in BJ and XD, which can be explained by the observed higher BVOC reactivity in TZ than the other two sites (see **Figure S9** and **Table S3**). Also, almost all the precursor groups showed positive RIR values, except negative RIR_{NO_x} appeared in BJ and XD in September. In addition, the RIR_{CO} values at the three sites suggested its limited role in O_3 formation at the three sites, compared with other major categories of O_3 precursors. Among the three subcategories of AVOC, alkenes* always had the highest RIR values, followed by aromatics, while the contribution of alkanes to O_3 formation can be ignored due to their near-zero RIR values. That sequence of O_3-AVOC sensitivity (alkenes* > aromatics > alkanes) indicated by the RIR analysis was consistent with previous studies in some other Chinese cities (Su et al., 2018b; Tan et al., 2019b). Significant monthly variations of O_3, NO_x, CO, VOC reactivity and TVOC/NO_x ratios (in ppbC/ppbv, as a widely used simple metric to determine the photochemical regime) (National Research Council, 1991) were also observed from May to September (see **Figure S9** and **Table S3**) at the three sites. For example, the BVOC reactivity in TZ showed highest level among the three sites during the whole campaign, and the AVOC reactivity in BJ showed more considerable variations in different months, which indicated spatial and temporal variations of local primary emission for O_3 precursors in Zibo city.

Figure 3c shows monthly RIR_{NO_x}/RIR_{AVOC} at each site, which clearly reveals the spatial and temporal variations in photochemical regimes. For instance, the photochemical regime at the TZ site was considered to be transitional regime in May, NO_x-limited regime in June and July, and VOC-limited regime in August and September; whereas for a specific month like June, NO_x-limited, VOC-limited, and transitional regimes were generally identified for TZ, BJ, and XD respectively. **Figure**

5b shows good consistency between monthly $TVOC/NO_x$ and RIR_{NOx}/RIR_{AVOC}, suggesting that the changes of local emissions for O_3 precursors may partially explain the considerable variation of O_3 formation chemistry in different months.

3.4 Week-to-week

Figure 4 shows the time series of week-to-week RIR values of major precursor groups and RIR_{NOx}/RIR_{AVOC} at three sites in Zibo. Compared with month-to-month results, **Figure 4** further reveals the O_3-precursor relationship with more information in temporal trends. The temporal variations in weekly RIR_{AVOC} at the three sites generally decreased and then increased, whereas weekly RIR_{NOx} represented an opposite temporal variation during the entire campaign. Additionally, weekly RIR_{BVOC} showed a trend of first decrease and then increase at TZ, while it did not show clear temporal variation at BJ and XD due to low values (**Figure 4a-c**). In general, $RIR_{alkanes}$, $RIR_{alkenes*}$ and $RIR_{aromatics}$ showed a tendency consistent with that of the RIR_{AVOC} at three sites (**Figure 4d-f**). Overall, these phenomena were consistent among the three sites, though the magnitude of RIR values varied site-to-site. In parallel, the temporal changing of O_3 precursor (e.g., AVOC, NO_x) was also observed at the three sites during the entire campaign (see **Figure S10**). For example, the weekly NO_x concentration showed an overall trend of first decrease and then increase, while the AVOC reactivity showed a different temporal variation. Given the moderate correlation between weekly $TVOC/NO_x$ and RIR_{AVOC}/RIR_{NOx} (**Figure 5c**), the temporal variations of RIR values and O_3 formation chemistry at the three sites may be partially elucidated by the emission changes of O_3 precursors.

As shown in **Figure 4g-i**, all the three sites showed similar temporal trends of RIR_{NOx}/RIR_{AVOC}, as it increased first and then decreased, though the magnitude of RIR_{NOx}/RIR_{AVOC} varied largely at each site. Such site-to-site variability of RIR_{NOx}/RIR_{AVOC} suggests that the photochemical regime in a local scale was mainly influenced by local emissions. By contrast, the site-to-site synchronization in temporal trend of RIR_{NOx}/RIR_{AVOC} suggests that the photochemical regime in a local scale may also be influenced by the emissions in a regional area. Therefore, the long-term, week-to-week RIR_{NOx}/RIR_{AVOC} of multiple sites can further reflect the variability of ozone formation regime at a large geographic scale.

3.5 Day-to-day

In this section, O_3-precursor relationship at the narrowest pattern of time scale was identified in detail. **Figure S11-S12** shows the time series of daily RIR values at three sites in Zibo, where the temporal trend of RIR values was consistent with that at weekly scale (**Figure 4**). Additionally, the time series of daily RIR_{NOx}/RIR_{AVOC} (**Figure S13**) showed more irregular variations in temporal trends during the entire campaign, though

376 such temporal trends were overall consistent with that of weekly scale in **Figure 4 g-i**.
377 In summary, the time series of RIR values from the daily scale can provide more
378 informative variations and characteristics of O_3-precursor relationship in temporal
379 trends.

380 **Table 2** summarizes the number of days and proportions that were classified into
381 the three photochemical regimes across each site and each pattern of time scale. Near-
382 consistent proportions of O_3 formation regimes (using RIR_{NOx}/RIR_{AVOC} as a metric)
383 were shown among multiple patterns of time scale, whereas a variability of proportion
384 occurred among the three sites. The proportions of photochemical regimes changed
385 accordingly along with the time scale varied from wider to narrower pattern. Taking TZ
386 as an example, 20% (monthly) and 26% (daily) of the time was considered as VOC-
387 limited regime. The number of days and proportions for photochemical regimes
388 summarized at four patterns of time scales can reveal a more plausible and
389 comprehensive variation in ozone formation chemistry. Compared with patterns of
390 monthly and weekly scales, the results derived at a daily scale can reveal the temporal
391 variability of photochemical regimes more comprehensively. Note that the
392 photochemical regime proportion obtained from the day-to-day scale has an advantage
393 due to the large number of statistical samples.

3.6 Comparison among different patterns of time scale

395 This section gives a more comprehensive understanding of the campaign-
396 averaging O_3-precursor relationship by comparing the similarities and differences of
397 the results from various patterns of time scale. The overall O_3-precursor relationship for
398 the entire campaign can be quantified by averaging the RIR values from the individual
399 simulation runs depending on the chosen time scale (e.g., five simulation runs for
400 monthly scale in this study). Therefore, four sets of logical and comparable results can
401 be derived to represent the campaign-averaging O_3-precursor relationship, as four
402 patterns of time scale (i.e., five-month, monthly, weekly, and daily) were treated in this
403 study.

404 **Figure 6** shows the averaged RIR values of the major precursor groups at different
405 patterns of time scale. As the time scale changed from wider (i.e., five-month scale) to
406 narrower (i.e., daily scale) pattern, all three sites showed increases in the means of
407 RIR_{AVOC} and $RIR_{alkenes*}$ as well as decreases in averaged RIR_{NOx}, whereas the averaged
408 RIR of other precursors (i.e., BVOC, CO, alkanes and aromatics) did not vary obviously
409 (see **Table S6**). Comparing with the O_3-VOC-NO_x sensitivity at the daily scale, the
410 results obtained at the five-month scale underestimated O_3-AVOC sensitivity (indicated
411 by averaged RIR values) by 48% (TZ), 66% (BJ), and 49% (XD), and overestimated
412 O_3-NO_x sensitivity by 37% (TZ), 142% (BJ), and 144% (XD). We performed
413 comprehensive uncertainty analysis for model input and output results, which was

414   assessed through statistical methods (see details in **Section 3.7**). We found that the
415   model-derived RIR values may become more uncertain when the input dataset was
416   averaged into a wider diurnal pattern (i.e., five-month scale), which may explain the
417   discrepancy of RIR values between five-month scale and daily scale. We expect that
418   such discrepancies derived from different patterns of time scale could widely exist in
419   many other world areas. Note that the mean RIR values were generally consistent
420   among the four patterns of time scale within a reasonable range (within 25-75th quantile
421   and standard deviation, see **Figure 6** and **Table S4**), suggesting that any selected pattern
422   of time scale could reasonably derive the campaign-averaging O_3-precursor relationship.
423   **Figure 7** further shows the variations in photochemical regimes (defined by
424   RIR_{NOx}/RIR_{AVOC}; see **Text S2** and **Table S4** for details) for each pattern of time scale.
425   Specifically, TZ was mainly considered as transitional regime for the entire campaign
426   period, whereas its variations covered three photochemical regimes, which was
427   consistent with the results from **Table S6**. BJ was generally identified as VOC-limited
428   regime, whereas some days were also grouped into transitional regime. XD was
429   considered as primarily between VOC-limited and transitional regime, and its
430   variations also spanned three photochemical regimes. Compared with the five-month
431   pattern, it was further found that the averaged RIR_{NOx}/RIR_{AVOC} from other time scale
432   patterns (i.e., monthly, weekly, and daily) were higher (12% to 20% for TZ; 38% to
433   153% for XD) or lower (21% to 65% for BJ) than that from five-month scale. Note that
434   the above discrepancies in photochemical regime derived from multiple patterns of time
435   scale may influence the development of targeted O_3 control strategies. In summary, the
436   photochemical regime derived by averaging RIR_{NOx}/RIR_{AVOC} from the daily scale (see
437   **Table S6**) suggests that the three sites mainly followed the sequence of TZ (1.34 $\pm$
438   1.39) > XD (0.67 $\pm$ 1.49) > BJ (0.16 $\pm$ 0.65).
439   In addition, the temporal variations of $TVOC/NO_x$ in different timescales were
440   identified during the whole campaign, and good correlations between observed
441    $TVOC/NO_x$ and model derived RIR_{NOx}/RIR_{AVOC} at four patterns of time scale were also
442   found (see **Figure 5**). Such consistency suggests that both metrics can reasonably
443   reflect the variation of photochemical regimes, which can also improve the reliability
444   of our box model simulation.
445   The consistency and difference of model output (summarized in **Table S7**) are
446   quantified by the statistical methods of Pearson's correlation coefficient (Hu et al., 2018)
447   and paired-samples *t*-test analysis (Wang et al., 2016). In particular, we assess and
448   compare the degree of significance of differences among multiple patterns of time scale
449   by the *p* values (a statistical significance assuming at $p < 0.05$) through paired-samples
450   *t*-test and Wilcoxon matched-paired signed-rank test (non-parametric statistics)
451   (Chiclana et al., 2013). **Figure 8a** shows high Pearson's correlation coefficients (with
452   values all above 0.85, $p < 0.01$) were found among four patterns of time scale, and the

higher correlation coefficient was identified between the two closer patterns. **Figure 8b-c** shows that the differences among multiple patterns of time scale were non-significant using Paired-samples t-test analysis and Wilcoxon matched-pair signed-rank test respectively. Furthermore, their results indicate that more significant difference was recognized between the two distant patterns (e.g., daily and five-month), which is consistent with the results of Pearson's correlation analysis. Noted that the discrepancy between the two distant patterns was not significant but non-negligible (e.g., $p = 0.092$ of Wilcoxon matched-paired signed-rank test between five-month and daily patterns).

The influence of different patterns of time scale on deriving RIR values from individual AVOC species was further investigated. Briefly, quantifying the relative contribution of individual AVOC on O_3 formation based on RIR calculation is beneficial to the development of cost-effective AVOC control strategies (Zhang et al., 2021). **Figure 9** shows the averaged RIR values of individual AVOC species (i.e., top 10) at different patterns of time scale (i.e., five-month, month-to-month, week-to-week) at three sites in Zibo. As shown in **Figure 9**, the 10 individual AVOC species at the three sites were selected according to the top 10 highest RIR from five-month pattern. All three sites showed that the RIR of individual AVOC species increased gradually as the time scale changed from the wider (i.e., five-month) to narrower (i.e., weekly) pattern, which was consistent with the earlier discussion (see **Figure 6** and **Table S6**) of O_3-AVOC sensitivity derived from four patterns of time scale. The results also indicate that the choice of time scale pattern has a limited effect on deriving high-ranking AVOC species (i.e., top 10) based on RIR calculations.

3.7 Uncertainty analysis

The uncertainty of model input was quantified in this section, which is embedded in pre-processed dataset with multiple patterns of time scale. As showed in **Figure 1**, the daily simulation used the individual daily pattern to constrain model, while the input dataset of averaged diurnal patterns (i.e., weekly, monthly, and five-month) is treated by averaging individual daily pattern into different timescales. This averaging approach will conceal the temporal variations of O_3 precursors and meteorological factors, particularly for a long-term observational campaign. **Figure S14** shows the distributions of the standard deviations for OH reactivity (k_{OH}) or concentration of O_3 precursor groups at three averaged patterns of time scale at the three sites. As the time scale changed from wider (i.e., five-month scale) to narrower (i.e., weekly scale) pattern, the uncertainty (indicated by the average, median and 25%-75% quantile) decreased accordingly. In addition, meteorological factors such as temperature and irradiation also play an important role on O_3 formation, especially these meteorological parameters can vary greatly over a long observational period (Boleti et al., 2020; Liu et al., 2019b; Weng et al., 2022). Therefore, the masked temporal variation of these meteorological

491 factors behind the averaged input dataset would also result in model uncertainty.

492   Moreover, it has been widely recognized that the uncertainty for 0-D box model
493 simulation mainly arises from the constraint of observation dataset and the
494 configuration of model scheme. Note that constraints with more species from
495 measurements (or including as many species as possible) would lower its uncertainty
496 from the chemical box model simulation (Wolfe et al., 2011, 2016). Nevertheless, due
497 to the measurement limitation in our field campaign, we are unable to measure some
498 important atmospheric species (i.e., HONO and oxygenated VOC (OVOC)), and these
499 may arise uncertainty in box model simulation. For instance, Xue et al., (2021)
500 performed a sensitivity test for HONO constraint in their box model simulation, and
501 they showed that without HONO constraint would lead to O_3 photochemical production
502 rate decreasing by 42%. More recently, Wang et al., (2022) obtained a comprehensive
503 VOC dataset at Guangzhou, and their results showed that box model simulation without
504 OVOCs constraints would underestimate the productions of ROx and O_3. Besides, both
505 gaseous HNO_3 and organic nitrates can result in interferences on NO_x measurement by
506 chemiluminescence technique, which may arise uncertainty in our box modelling (Ge
507 et al., 2022; Uno et al., 2017; Xu et al., 2013). Since the accurate NO_x measurement is
508 essential in determining the photochemical regime, more in-depth studies on NO_x
509 measurement uncertainty in box model simulation are required in the future. In addition,
510 the parameter configuration of model scheme is essential to derive a reliable and valid
511 model output, such as dilution rate as an important model technical parameter. We
512 performed a stepwise sensitivity test for this parameter to obtain an optimized dilution
513 rate, and assigned it to all non-constraint species, which can reduce uncertainty in box
514 model simulation (see details in **Text S1**). Also, the dry and/or wet deposition of
515 pollutants is an important atmospheric physical process, which has been mostly
516 parameterized in emission-based chemical transport modeling but very limited in box
517 model, as most of the primarily emitted species are already constrained from
518 measurements. Xue et al., (2014) considered O_3 deposition into box model simulation,
519 and their result showed negligible contribution of O_3 deposition to total O_3 destruction
520 rates. As for this work, we are unable to consider the deposition due to the difficulty in
521 representing and parameterizing this term in the 0-D box model. Nevertheless,
522 deposition of O_3 and other species may be one of the uncertainties during box model
523 simulation, which is worth further study in the future.

524 **4 Summary and implications**

525   Our present results suggest that comprehensively understanding of multiple
526 patterns of time scale is conductive to formulating a more accurate and robust O_3 control
527 strategy. Specifically, as identified from the narrower patterns of time scale (i.e., weekly
528 and daily), the site-to-site photochemical regime indicated by RIR_{NOx}/RIR_{AVOC} showed

various magnitudes but a synchronous temporal trend. This indicates that the O_3 formation regime in a city area can be influenced by local and regional emissions jointly. The reason behind this phenomenon is not clear at present, and we believe that further investigation on the synergetic effect of local and regional emission reduction for O_3 control would help elucidating this observation. It was also found that the campaign-averaging photochemical regimes showed overall consistency but non-negligible variability among the four patterns of time scale, which was mainly due to the embedded uncertainty in model input dataset with averaged diurnal patterns. This implies that comparison among multiple patterns of time scale based on RIR analysis is useful to derive the O_3-precursor relationship more accurately and reliably.

Moreover, the high-ranking AVOC species (i.e., top 10) based on RIR calculations were overall consistent from the narrow to wide patterns of time scale. **Table S8** summarizes the total run number of box model for different patterns of time scale. It is known that large-scale computing capacity and computational efficiency were required in the narrower pattern of time scale (e.g., 2760 simulation runs in weekly scale in this study). Considering the difficulties of performing long-term and continuous online measurements in some environments, it is also advisable to identify the high-ranking VOC species from the campaign-averaging diurnal pattern in box model simulation.

In this study, we explored the non-linearity of O_3-precursor relationship in a way driven by the actual daily / weekly / monthly variability around the distribution. Our results highlight the importance to quantitatively test the impact of different timescales on photochemical regime determination, as there is uncertainty embedded in model input dataset when averaging individual daily pattern into different timescales. Such understanding would be complementary in developing more accurate O_3 pollution control strategy, particularly as the long-term O_3-precursor observations (e.g., from several months to years) are becoming more available than before in many places of China. In addition, site-to-site differences of model-derived photochemical regimes also underlines the importance of developing target O_3 control strategy for different areas in a city scale. Specifically, according to the averaged RIR_{NOx}/RIR_{AVOC} at daily pattern, the derived photochemical regime was transitional for TZ (suburban) and XD (suburban), while VOC-limited for BJ (urban). This implies that for mitigating ozone pollution in Zibo city, more endeavors should be devoted to the anthropogenic VOC reduction in urban areas, while strengthening the synergetic mitigation of VOC and NO_x emissions at the same time in other suburban areas. Although the above implications for O_3 control were derived from a case study in a major prefecture-level city (Zibo) of northern China, the developed approach by integrating multiple patterns of time scale in the present work can be used to other regions, particularly the on-going "One City One Policy" campaign (2021-2023) for O_3 control in many cities in China.

Code availability

The code for the Master Chemical Mechanism (MCMv3.3.1) can be achieved from http://mcm.york.ac.uk (last access: 27 January 2023).

Data availability

The datasets generated and analysed during the current study are available on reasonable request from the corresponding author (Kangwei Li).

Supplement

The supplement related to this article is available online.

Author contribution

KL conceived and led the study. ZZ performed the modeling. ZZ, KL, and ZB analyzed the data. BX, JD, LL, GZ, SL, CG, and WY conducted the field measurement. ZZ and KL wrote the paper. MA and ZB commented on the manuscript.

Competing interests

The authors declare that they have no conflicts of interest.

Acknowledgement

We thank Prof. William Bloss for initial check and helpful comments.

Financial support

This work was supported by National Center for Air Pollution Prevention and Control (No. DQGG202119) and Ministry of Science and Technology PRC (No. G20200160001, No. G2021060002L).

References

Blanchard, C. L.: Ozone process insights from field experiments – Part III: extent of reaction and ozone formation, Atmos. Environ., 34(12), 2035–2043, doi:https://doi.org/10.1016/S1352-2310(99)00458-6, 2000.

Boleti, E., Hueglin, C., Grange, S. K., Prévôt, A. S. H. and Takahama, S.: Temporal and spatial analysis of ozone concentrations in Europe based on timescale decomposition and a multi-clustering approach, Atmos. Chem. Phys., 20(14), 9051–9066, doi:10.5194/acp-20-9051-2020, 2020.

Brunekreef, B. and Holgate, S. T.: Air pollution and health, Lancet, 360(9341), 1233–1242, doi:10.1016/S0140-6736(02)11274-8, 2002.

Cardelino, C. A. and Chameides, W. L.: An observation-based model for analyzing ozone precursor relationships in the urban atmosphere, J. Air Waste Manag. Assoc., 45(3), 161–180, doi:10.1080/10473289.1995.10467356, 1995.

Carter, W. P. L.: Development of the SAPRC-07 chemical mechanism, Atmos. Environ., 44(40), 5324–5335, doi:https://doi.org/10.1016/j.atmosenv.2010.01.026, 2010.

Cheng, H., Guo, H., Wang, X., Saunders, S. M., Lam, S. H. M., Jiang, F., Wang, T., Ding, A., Lee, S. and Ho, K. F.: On the relationship between ozone and its precursors in the Pearl River Delta: Application of an observation-based model (OBM), Environ. Sci. Pollut. Res., 17(3), 547–560, doi:10.1007/s11356-009-0247-9, 2010.

Chiclana, F., García, J. M. T., del Moral, M. J. and Herrera-Viedma, E.: A statistical comparative study of different similarity measures of consensus in group decision making, Inf. Sci. (Ny)., 221, 110–123, 2013.

Chien, Y.-C.: Variations in amounts and potential sources of volatile organic chemicals in new cars, Sci. Total Environ., 382(2), 228–239, doi:https://doi.org/10.1016/j.scitotenv.2007.04.022, 2007.

Council, N. R.: Rethinking the Ozone Problem in Urban and Regional Air Pollution, The National Academies Press, Washington, DC., 1991.

Fan, M. Y., Zhang, Y. L., Lin, Y. C., Li, L., Xie, F., Hu, J., Mozaffar, A. and Cao, F.: Source apportionments of atmospheric volatile organic compounds in Nanjing, China during high ozone pollution season, Chemosphere, 263, 128025, doi:10.1016/j.chemosphere.2020.128025, 2021.

Ge, D., Nie, W., Sun, P., Liu, Y., Wang, T., Wang, J., Wang, J., Wang, L., Zhu, C. and Wang, R.: Characterization of particulate organic nitrates in the Yangtze River Delta, East China, using the time-of-flight aerosol chemical speciation monitor, Atmos. Environ., 272, 118927, 2022.

Goliff, W. S., Stockwell, W. R. and Lawson, C. V: The regional atmospheric chemistry mechanism, version 2, Atmos. Environ., 68, 174–185, doi:https://doi.org/10.1016/j.atmosenv.2012.11.038, 2013.

He, Z., Wang, X., Ling, Z., Zhao, J., Guo, H., Shao, M. and Wang, Z.: Contributions of

different anthropogenic volatile organic compound sources to ozone formation at a receptor site in the Pearl River Delta region and its policy implications, Atmos. Chem. Phys., 19(13), 8801–8816, doi:10.5194/acp-19-8801-2019, 2019a.

He, Z., Wang, X., Ling, Z., Zhao, J., Guo, H., Shao, M. and Wang, Z.: Contributions of different anthropogenic volatile organic compound sources to ozone formation at a receptor site in the Pearl River Delta region and its policy implications, Atmos. Chem. Phys., 19(13), 8801–8816, doi:10.5194/acp-19-8801-2019, 2019b.

Hidy, G. M.: Ozone process insights from field experiments - part I: Overview, Atmos. Environ., 34(12–14), 2001–2022, doi:10.1016/S1352-2310(99)00456-2, 2000.

Hu, H., Landgraf, J., Detmers, R., Borsdorff, T., Aan de Brugh, J., Aben, I., Butz, A. and Hasekamp, O.: Toward global mapping of methane with TROPOMI: First results and intersatellite comparison to GOSAT, Geophys. Res. Lett., 45(8), 3682–3689, 2018.

Jenkin, M. E., Young, J. C. and Rickard, A. R.: The MCM v3.3.1 degradation scheme for isoprene, Atmos. Chem. Phys., 15(20), 11433–11459, doi:10.5194/acp-15-11433-2015, 2015.

Jiang, M., Lu, K., Su, R., Tan, Z., Wang, H., Li, L., Fu, Q., Zhai, C., Tan, Q. and Yue, D.: Ozone formation and key VOCs in typical Chinese city clusters, Chinese Sci. Bull., 63(12), 1130–1141, 2018.

Kleinman, L. I.: Ozone process insights from field experiments – part II: Observation-based analysis for ozone production, Atmos. Environ., 34(12), 2023–2033, doi:https://doi.org/10.1016/S1352-2310(99)00457-4, 2000.

Li, J., Zhai, C., Yu, J., Liu, R., Li, Y., Zeng, L. and Xie, S.: Spatiotemporal variations of ambient volatile organic compounds and their sources in Chongqing, a mountainous megacity in China, Sci. Total Environ., 627, 1442–1452, 2018.

Li, K., Jacob, D. J., Liao, H., Shen, L., Zhang, Q. and Bates, K. H.: Anthropogenic drivers of 2013–2017 trends in summer surface ozone in China, Proc. Natl. Acad. Sci., 116(2), 422 LP – 427, doi:10.1073/pnas.1812168116, 2019.

Li, K., Wang, X., Li, L., Wang, J., Liu, Y., Cheng, X., Xu, B., Wang, X., Yan, P., Li, S., Geng, C., Yang, W., Azzi, M. and Bai, Z.: Large variability of O3-precursor relationship during severe ozone polluted period in an industry-driven cluster city (Zibo) of North China Plain, J. Clean. Prod., 316, 128252, doi:https://doi.org/10.1016/j.jclepro.2021.128252, 2021.

Lin, H., Wang, M., Duan, Y., Fu, Q., Ji, W., Cui, H., Jin, D., Lin, Y. and Hu, K.: O3 sensitivity and contributions of different nmhc sources in O3 formation at urban and suburban sites in Shanghai, Atmosphere (Basel)., 11(3), 295, 2020.

Ling, Z. H., Guo, H., Cheng, H. R. and Yu, Y. F.: Sources of ambient volatile organic compounds and their contributions to photochemical ozone formation at a site in the Pearl River Delta, southern China, Environ. Pollut., 159(10), 2310–2319, doi:10.1016/j.envpol.2011.05.001, 2011.

Liu, X., Lyu, X., Wang, Y., Jiang, F. and Guo, H.: Intercomparison of O3 formation and radical chemistry in the past decade at a suburban site in Hong Kong, Atmos.

675   Chem. Phys., 19(7), 5127–5145, doi:10.5194/acp-19-5127-2019, 2019a.

676   Liu, X., Lyu, X., Wang, Y., Jiang, F. and Guo, H.: Intercomparison of O3 formation
677   and radical chemistry in the past decade at a suburban site in Hong Kong, Atmos.
678   Chem. Phys., 19(7), 5127–5145, doi:10.5194/acp-19-5127-2019, 2019b.

679   Liu, X., Wang, N., Lyu, X., Zeren, Y., Jiang, F., Wang, X., Zou, S., Ling, Z. and Guo,
680   H.: Photochemistry of ozone pollution in autumn in Pearl River Estuary, South
681   China, Sci. Total Environ., 754, 141812,
682   doi:https://doi.org/10.1016/j.scitotenv.2020.141812, 2021a.

683   Liu, X., Wang, N., Lyu, X., Zeren, Y., Jiang, F., Wang, X., Zou, S., Ling, Z. and Guo,
684   H.: Photochemistry of ozone pollution in autumn in Pearl River Estuary, South
685   China, Sci. Total Environ., 754, doi:10.1016/j.scitotenv.2020.141812, 2021b.

686   Lu, H., Lyu, X., Cheng, H., Ling, Z., Guo, H. and Lu, H.: Overview on the spatial–
687   temporal characteristics of the ozone formation regime in China, Environ. Sci., v.
688   21(6), 916-929–2019 v.21 no.6, doi:10.1039/c9em00098d, 2019.

689   Lu, K., Zhang, Y., Su, H., Brauers, T., Chou, C. C., Hofzumahaus, A., Liu, S. C., Kita,
690   K., Kondo, Y., Shao, M., Wahner, A., Wang, J., Wang, X. and Zhu, T.: Oxidant
691   (O3 + NO2) production processes and formation regimes in Beijing, J. Geophys.
692   Res. Atmos., 115(7), 1–18, doi:10.1029/2009JD012714, 2010a.

693   Lu, K., Zhang, Y., Su, H., Shao, M., Zeng, L., Zhong, L., Xiang, Y., Chang, C., Chou,
694   C. K. C. and Wahner, A.: Regional ozone pollution and key controlling factors of
695   photochemical ozone production in Pearl River Delta during summer time, Sci.
696   China Chem., 53(3), 651–663, doi:10.1007/s11426-010-0055-6, 2010b.

697   Lu, X., Hong, J., Zhang, L., Cooper, O. R., Schultz, M. G., Xu, X., Wang, T., Gao, M.,
698   Zhao, Y. and Zhang, Y.: Severe Surface Ozone Pollution in China: A Global
699   Perspective, Environ. Sci. Technol. Lett., 5(8), 487–494,
700   doi:10.1021/acs.estlett.8b00366, 2018.

701   Lyu, X., Wang, N., Guo, H., Xue, L., Jiang, F., Zeren, Y., Cheng, H., Cai, Z., Han, L.
702   and Zhou, Y.: Causes of a continuous summertime O3 pollution event in Jinan, a
703   central city in the North China Plain, Atmos. Chem. Phys., 19(5), 3025–3042,
704   doi:10.5194/acp-19-3025-2019, 2019a.

705   Lyu, X., Wang, N., Guo, H., Xue, L., Jiang, F., Zeren, Y., Cheng, H., Cai, Z., Han, L.
706   and Zhou, Y.: Causes of a continuous summertime O3 pollution event in Jinan, a
707   central city in the North China Plain, Atmos. Chem. Phys., 19(5), 3025–3042,
708   doi:10.5194/acp-19-3025-2019, 2019b.

709   Lyu, X. P., Chen, N., Guo, H., Zhang, W. H., Wang, N., Wang, Y. and Liu, M.: Ambient
710   volatile organic compounds and their effect on ozone production in Wuhan, central
711   China, Sci. Total Environ., 541, 200–209,
712   doi:https://doi.org/10.1016/j.scitotenv.2015.09.093, 2016a.

713   Lyu, X. P., Chen, N., Guo, H., Zhang, W. H., Wang, N., Wang, Y. and Liu, M.: Ambient
714   volatile organic compounds and their effect on ozone production in Wuhan, central
715   China, Sci. Total Environ., 541, 200–209, doi:10.1016/j.scitotenv.2015.09.093,
716   2016b.

717 Qin, M., Chen, Z., Shen, H., Li, H., Wu, H. and Wang, Y.: Impacts of heterogeneous
718   reactions to atmospheric peroxides: Observations and budget analysis study, Atmos.
719   Environ., 183(April), 144–153, doi:10.1016/j.atmosenv.2018.04.005, 2018.
720 Saunders, S. M., Jenkin, M. E., Derwent, R. G. and Pilling, M. J.: Protocol for the
721   development of the Master Chemical Mechanism, MCM v3 (Part A): Tropospheric
722   degradation of non-aromatic volatile organic compounds, Atmos. Chem. Phys., 3(1),
723   161–180, doi:10.5194/acp-3-161-2003, 2003.
724 Sicard, P., De Marco, A., Agathokleous, E., Feng, Z., Xu, X., Paoletti, E., Rodriguez,
725   J. J. D. and Calatayud, V.: Amplified ozone pollution in cities during the COVID-
726   19 lockdown, Sci. Total Environ., 735, doi:10.1016/j.scitotenv.2020.139542, 2020.
727 Sillman, S.: Observation-Based Methods (OBMS) For Analyzing Urban/Regional
728   Ozone Production And Ozone-NO_x-VOC Sensitivity. Available from: http://www-
729   personal.engin.umich.edu/~sillman, 2010.
730 Stockwell, W. R., Kirchner, F., Kuhn, M. and Seefeld, S.: A new mechanism for
731   regional atmospheric chemistry modeling, J. Geophys. Res. Atmos., 102(22),
732   doi:10.1029/97jd00849, 1997.
733 Stockwell, W. R., Saunders, E., Goliff, W. S. and Fitzgerald, R. M.: A perspective on
734   the development of gas-phase chemical mechanisms for Eulerian air quality models,
735   J. Air Waste Manage. Assoc., 70(1), 44–70, 2020.
736 Su, R., Lu, K., Yu, J., Tan, Z., Jiang, M., Li, J., Xie, S., Wu, Y., Zeng, L. and Zhai, C.:
737   Exploration of the formation mechanism and source attribution of ambient ozone in
738   Chongqing with an observation-based model, Sci. China Earth Sci., 61(1), 23–32,
739   2018a.
740 Su, R., Lu, K. D., Yu, J. Y., Tan, Z. F., Jiang, M. Q., Li, J., Xie, S. D., Wu, Y. S., Zeng,
741   L. M., Zhai, C. Z. and Zhang, Y. H.: Exploration of the formation mechanism and
742   source attribution of ambient ozone in Chongqing with an observation-based model,
743   Sci. China Earth Sci., 61(1), 23–32, doi:10.1007/s11430-017-9104-9, 2018b.
744 Sun, L., Xue, L., Wang, T., Gao, J., Ding, A., Cooper, O. R., Lin, M., Xu, P., Wang, Z.,
745   Wang, X., Wen, L., Zhu, Y., Chen, T., Yang, L., Wang, Y., Chen, J. and Wang, W.:
746   Significant increase of summertime ozone at Mount Tai in Central Eastern China,
747   Atmos. Chem. Phys., 16(16), 10637–10650, doi:10.5194/acp-16-10637-2016, 2016.
748 Tan, Z., Lu, K., Dong, H., Hu, M., Li, X., Liu, Y., Lu, S., Shao, M., Su, R. and Wang,
749   H.: Explicit diagnosis of the local ozone production rate and the ozone-NO_x-VOC
750   sensitivities, Sci. Bull., 63(16), 1067–1076, 2018a.
751 Tan, Z., Lu, K., Jiang, M., Su, R., Dong, H., Zeng, L., Xie, S., Tan, Q. and Zhang, Y.:
752   Exploring ozone pollution in Chengdu, southwestern China: A case study from
753   radical chemistry to O3-VOC-NO_x sensitivity, Sci. Total Environ., 636, 775–786,
754   2018b.
755 Tan, Z., Lu, K., Jiang, M., Su, R., Wang, H., Lou, S., Fu, Q., Zhai, C., Tan, Q. and Yue,
756   D.: Daytime atmospheric oxidation capacity in four Chinese megacities during the
757   photochemically polluted season: a case study based on box model simulation,
758   Atmos. Chem. Phys., 19(6), 3493–3513, 2019a.

Tan, Z., Lu, K., Jiang, M., Su, R., Wang, H., Lou, S., Fu, Q., Zhai, C., Tan, Q., Yue, D., Chen, D., Wang, Z., Xie, S., Zeng, L. and Zhang, Y.: Daytime atmospheric oxidation capacity in four Chinese megacities during the photochemically polluted season: A case study based on box model simulation, Atmos. Chem. Phys., 19(6), 3493–3513, doi:10.5194/acp-19-3493-2019, 2019b.

Uno, I., Osada, K., Yumimoto, K., Wang, Z., Itahashi, S., Pan, X., Hara, Y., Kanaya, Y., Yamamoto, S. and Fairlie, T. D.: Seasonal variation of fine-and coarse-mode nitrates and related aerosols over East Asia: synergetic observations and chemical transport model analysis, Atmos. Chem. Phys., 17(23), 14181–14197, 2017.

Vingarzan, R.: A review of surface ozone background levels and trends, Atmos. Environ., 38(21), 3431–3442, 2004.

Wang, H., Hu, X. and Sterba-Boatwright, B.: A new statistical approach for interpreting oceanic fCO2 data, Mar. Chem., 183, 41–49, 2016.

Wang, M., Hu, K., Chen, W., Shen, X., Li, W. and Lu, X.: Ambient Non-Methane Hydrocarbons (NMHCs) Measurements in Baoding, China: Sources and Roles in Ozone Formation, Atmosphere (Basel)., 11(11), 1205, 2020a.

Wang, P., Chen, Y., Hu, J., Zhang, H. and Ying, Q.: Attribution of Tropospheric Ozone to NO x and VOC Emissions: Considering Ozone Formation in the Transition Regime, Environ. Sci. Technol., 53(3), 1404–1412, doi:10.1021/acs.est.8b05981, 2019.

Wang, T., Xue, L., Brimblecombe, P., Lam, Y. F., Li, L. and Zhang, L.: Ozone pollution in China: A review of concentrations, meteorological influences, chemical precursors, and effects, Sci. Total Environ., 575, 1582–1596, doi:10.1016/j.scitotenv.2016.10.081, 2017a.

Wang, T., Xue, L., Brimblecombe, P., Lam, Y. F., Li, L. and Zhang, L.: Ozone pollution in China: A review of concentrations, meteorological influences, chemical precursors, and effects, Sci. Total Environ., 575, 1582–1596, 2017b.

Wang, W., Yuan, B., Peng, Y., Su, H., Cheng, Y., Yang, S., Wu, C., Qi, J., Bao, F. and Huangfu, Y.: Direct observations indicate photodegradable oxygenated volatile organic compounds (OVOCs) as larger contributors to radicals and ozone production in the atmosphere, Atmos. Chem. Phys., 22(6), 4117–4128, 2022.

Wang, Y., Wang, H., Guo, H., Lyu, X., Cheng, H., Ling, Z., Louie, P. K. K., Simpson, I. J., Meinardi, S. and Blake, D. R.: Long-term O 3–precursor relationships in Hong Kong: field observation and model simulation, Atmos. Chem. Phys., 17(18), 10919–10935, 2017c.

Wang, Y., Wang, H., Guo, H., Lyu, X., Cheng, H., Ling, Z., Louie, P. K. K., Simpson, I. J., Meinardi, S. and Blake, D. R.: Long-term O3-precursor relationships in Hong Kong: Field observation and model simulation, Atmos. Chem. Phys., 17(18), 10919–10935, doi:10.5194/acp-17-10919-2017, 2017d.

Wang, Y., Guo, H., Zou, S., Lyu, X., Ling, Z., Cheng, H. and Zeren, Y.: Surface O3 photochemistry over the South China Sea: Application of a near-explicit chemical mechanism box model, Environ. Pollut., 234, 155–166,

801   doi:10.1016/j.envpol.2017.11.001, 2018.

802   Wang, Y., Gao, W., Wang, S., Song, T., Gong, Z., Ji, D., Wang, L., Liu, Z., Tang, G.,
803   Huo, Y., Tian, S., Li, J., Li, M., Yang, Y., Chu, B., Petäjä, T., Kerminen, V. M., He,
804   H., Hao, J., Kulmala, M., Wang, Y. and Zhang, Y.: Contrasting trends of PM2.5and
805   surface-ozone concentrations in China from 2013 to 2017, Natl. Sci. Rev., 7(8),
806   1331–1339, doi:10.1093/nsr/nwaa032, 2020b.

807   Weng, X., Forster, G. L. and Nowack, P.: A machine learning approach to quantify
808   meteorological drivers of ozone pollution in China from 2015 to 2019, Atmos.
809   Chem. Phys., 22(12), 8385–8402, doi:10.5194/acp-22-8385-2022, 2022.

810   Whalley, L. K., Slater, E. J., Woodward-Massey, R., Ye, C., Lee, J. D., Squires, F.,
811   Hopkins, J. R., Dunmore, R. E., Shaw, M. and Hamilton, J. F.: Evaluating the
812   sensitivity of radical chemistry and ozone formation to ambient VOCs and NO x in
813   Beijing, Atmos. Chem. Phys., 21(3), 2125–2147, 2021a.

814   Whalley, L. K., Slater, E. J., Woodward-Massey, R., Ye, C., Lee, J. D., Squires, F.,
815   Hopkins, J. R., Dunmore, R. E., Shaw, M., Hamilton, J. F., Lewis, A. C., Mehra,
816   A., Worrall, S. D., Bacak, A., Bannan, T. J., Coe, H., Percival, C. J., Ouyang, B.,
817   Jones, R. L., Crilley, L. R., Kramer, L. J., Bloss, W. J., Vu, T., Kotthaus, S.,
818   Grimmond, S., Sun, Y., Xu, W., Yue, S., Ren, L., Joe, W., Nicholas Hewitt, C.,
819   Wang, X., Fu, P. and Heard, D. E.: Evaluating the sensitivity of radical chemistry
820   and ozone formation to ambient VOCs and NO$_x$ in Beijing, Atmos. Chem. Phys.,
821   21(3), 2125–2147, doi:10.5194/acp-21-2125-2021, 2021b.

822   Willmott, C. J.: Some comments on the evaluation of model performance., Bull. - Am.
823   Meteorol.   Soc.,   63(11),   1309–1313,   doi:10.1175/1520-
824   0477(1982)063<1309:SCOTEO>2.0.CO;2, 1982.

825   Wolfe, G. M., Thornton, J. A., Bouvier-Brown, N. C., Goldstein, A. H., Park, J.-H.,
826   McKay, M., Matross, D. M., Mao, J., Brune, W. H. and LaFranchi, B. W.: The
827   Chemistry of Atmosphere-Forest Exchange (CAFE) model–part 2: application to
828   BEARPEX-2007 observations, Atmos. Chem. Phys., 11(3), 1269–1294, 2011.

829   Wolfe, G. M., Marvin, M. R., Roberts, S. J., Travis, K. R. and Liao, J.: The framework
830   for 0-D atmospheric modeling (F0AM) v3. 1, Geosci. Model Dev., 9(9), 3309–3319,
831   2016.

832   Xie, X., Shao, M., Liu, Y., Lu, S., Chang, C.-C. and Chen, Z.-M.: Estimate of initial
833   isoprene contribution to ozone formation potential in Beijing, China, Atmos.
834   Environ., 42(24), 6000–6010, 2008.

835   Xu, Z., Wang, T., Xue, L. K., Louie, P. K. K., Luk, C. W. Y., Gao, J., Wang, S. L.,
836   Chai, F. H. and Wang, W. X.: Evaluating the uncertainties of thermal catalytic
837   conversion in measuring atmospheric nitrogen dioxide at four differently polluted
838   sites in China, Atmos. Environ., 76, 221–226, 2013.

839   Xu, Z., Huang, X., Nie, W., Chi, X., Xu, Z., Zheng, L., Sun, P. and Ding, A.: Influence
840   of synoptic condition and holiday effects on VOCs and ozone production in the
841   Yangtze River Delta region, China, Atmos. Environ., 168, 112–124, 2017.

842   Xue, L., Wang, T., Louie, P. K. K., Luk, C. W. Y., Blake, D. R. and Xu, Z.: Increasing

843 external effects negate local efforts to control ozone air pollution: a case study of
844 Hong Kong and implications for other Chinese cities, Environ. Sci. Technol.,
845 48(18), 10769–10775, 2014a.

846 Xue, L., Wang, T., Louie, P. K. K., Luk, C. W. Y., Blake, D. R. and Xu, Z.: Increasing
847 external effects negate local efforts to control ozone air pollution: A case study of
848 Hong Kong and implications for other chinese cities, Environ. Sci. Technol., 48(18),
849 10769–10775, doi:10.1021/es503278g, 2014b.

850 Xue, L. K., Wang, T., Gao, J., Ding, A. J., Zhou, X. H., Blake, D. R., Wang, X. F.,
851 Saunders, S. M., Fan, S. J., Zuo, H. C., Zhang, Q. Z. and Wang, W. X.: Ground-
852 level ozone in four Chinese cities: Precursors, regional transport and heterogeneous
853 processes, Atmos. Chem. Phys., 14(23), 13175–13188, doi:10.5194/acp-14-13175-
854 2014, 2014c.

855 Xue, M., Ma, J., Tang, G., Tong, S., Hu, B., Zhang, X., Li, X. and Wang, Y.: ROx
856 Budgets and O3 Formation during Summertime at Xianghe Suburban Site in the
857 North China Plain, Adv. Atmos. Sci., 38(7), 1209–1222, 2021.

858 Xue, T., Zheng, Y., Geng, G., Xiao, Q., Meng, X., Wang, M., Li, X., Wu, N., Zhang,
859 Q. and Zhu, T.: Estimating Spatiotemporal Variation in Ambient Ozone Exposure
860 during 2013–2017 Using a Data-Fusion Model, Environ. Sci. Technol., 54(23),
861 14877–14888, 2020.

862 Yarwood, G., Rao, S., Yocke, M. and Whitten, G. Z.: Updates to the carbon bond
863 chemical mechanism: CB05, Final Rep. to US EPA, RT-0400675, 8, 13, 2005.

864 Yarwood, G., Jung, J., Whitten, G. Z., Heo, G., Mellberg, J. and Estes, M.: Updates to
865 the Carbon Bond mechanism for version 6 (CB6), in 9th Annual CMAS Conference,
866 Chapel Hill, NC, pp. 11–13., 2010.

867 Yin, M., Zhang, X., Li, Y., Fan, K., Li, H., Gao, R. and Li, J.: Ambient ozone pollution
868 at a coal chemical industry city in the border of Loess Plateau and Mu Us Desert:
869 characteristics, sensitivity analysis and control strategies, PeerJ, 9, e11322, 2021.

870 Yu, D., Tan, Z., Lu, K., Ma, X., Li, X., Chen, S., Zhu, B., Lin, L., Li, Y., Qiu, P., Yang,
871 X., Liu, Y., Wang, H., He, L., Huang, X. and Zhang, Y.: An explicit study of local
872 ozone budget and NO_x-VOCs sensitivity in Shenzhen China, Atmos. Environ., 224,
873 117304, doi:https://doi.org/10.1016/j.atmosenv.2020.117304, 2020a.

874 Yu, D., Tan, Z., Lu, K., Ma, X., Li, X., Chen, S., Zhu, B., Lin, L., Li, Y., Qiu, P., Yang,
875 X., Liu, Y., Wang, H., He, L., Huang, X. and Zhang, Y.: An explicit study of local
876 ozone budget and NO_x-VOCs sensitivity in Shenzhen China, Atmos. Environ.,
877 224(November 2019), 117304, doi:10.1016/j.atmosenv.2020.117304, 2020b.

878 Zeng, L., Lyu, X., Guo, H., Zou, S. and Ling, Z.: Photochemical Formation of C1-C5
879 Alkyl Nitrates in Suburban Hong Kong and over the South China Sea, Environ. Sci.
880 Technol., 52(10), 5581–5589, doi:10.1021/acs.est.8b00256, 2018.

881 Zhang, Q., Zheng, Y., Tong, D., Shao, M., Wang, S., Zhang, Y., Xu, X., Wang, J., He,
882 H., Liu, W., Ding, Y., Lei, Y., Li, J., Wang, Z., Zhang, X., Wang, Y., Cheng, J.,
883 Liu, Y., Shi, Q., Yan, L., Geng, G., Hong, C., Li, M., Liu, F., Zheng, B., Cao, J.,
884 Ding, A., Gao, J., Fu, Q., Huo, J., Liu, B., Liu, Z., Yang, F., He, K. and Hao, J.:

885   Drivers of improved PM2.5 air quality in China from 2013 to 2017, Proc. Natl.
886   Acad. Sci., 116(49), 24463 LP – 24469, doi:10.1073/pnas.1907956116, 2019.

887   Zhang, Y., Xue, L., Carter, W. P. L., Pei, C., Chen, T., Mu, J., Wang, Y., Zhang, Q. and
888   Wang, W.: Development of ozone reactivity scales for volatile organic compounds
889   in a Chinese megacity, Atmos. Chem. Phys., 21(14), 11053–11068,
890   doi:10.5194/acp-21-11053-2021, 2021.

891   Zhang, Y. H., Hu, M., Zhong, L. J., Wiedensohler, A., Liu, S. C., Andreae, M. O., Wang,
892   W. and Fan, S. J.: Regional Integrated Experiments on Air Quality over Pearl River
893   Delta 2004 (PRIDE-PRD2004): Overview, Atmos. Environ., 42(25), 6157–6173,
894   doi:10.1016/j.atmosenv.2008.03.025, 2008a.

895   Zhang, Y. H., Su, H., Zhong, L. J., Cheng, Y. F., Zeng, L. M., Wang, X. S., Xiang, Y.
896   R., Wang, J. L., Gao, D. F., Shao, M., Fan, S. J. and Liu, S. C.: Regional ozone
897   pollution and observation-based approach for analyzing ozone–precursor
898   relationship during the PRIDE-PRD2004 campaign, Atmos. Environ., 42(25),
899   6203–6218, doi:https://doi.org/10.1016/j.atmosenv.2008.05.002, 2008b.

900   Zhao, Y., Chen, L., Li, K., Han, L., Zhang, X., Wu, X., Gao, X., Azzi, M. and Cen, K.:
901   Atmospheric ozone chemistry and control strategies in Hangzhou, China:
902   Application of a 0-D box model, Atmos. Res., 246, 105109, 2020.

903   Zong, R., Yang, X., Wen, L., Xu, C., Zhu, Y., Chen, T., Yao, L., Wang, L., Zhang, J.,
904   Yang, L., Wang, X., Shao, M., Zhu, T., Xue, L. and Wang, W.: Strong ozone
905   production at a rural site in theNorth China Plain: Mixed effects of urban plumesand
906   biogenic emissions, J. Environ. Sci. (China), 71, 261–270,
907   doi:10.1016/j.jes.2018.05.003, 2018.

908

909

Table 1. Summary of relevant published 0-D box model studies in China.

City	Site/Type		Period	Patterns of Time scale[a]	Mechanism	Reference
Beijing	PKU[b]	Urban	10 Aug–10 Sep 2006	Day-to-day (25 d)	CB-IV	(Lu et al., 2010)
	YUFA	Suburban	13–29 Apr 2015, 11–29 Aug 2015, 22 Feb–12 Mar 2016	Entire period	RACM2	(Qin et al., 2018)
	PKU	Urban	2–19 Jul 2014	Entire period	RACM2	(Tan et al., 2019b)
	Beijing	Urban	1 Jun–6 Jul 2013	Day-to-day (2 d)	MCMv3.3.1	(Zong et al., 2018)
Dezhou	Yucheng	Rural	28 Sep–31 Oct 2018	Entire period	RACM2	(Yu et al., 2020b)
Shenzhen	SYY[c]	Urban	10 Aug–21 Oct 2013	Entire period	MCMv3.2	(Zeng et al., 2018)
	Fucheng	Urban				
Hong Kong	TC	Suburban	Sep-Nov 2002, 2007, 2012	Year-to-year (3 yrs)	MCMv3.2	(Xue et al., 2014b)
	Wan Shan	Island				
	Tung Chung	Urban				
	Qing Sha	Urban				
	Tai O	Urban	23 Oct–1 Nov 2007	Day-to-day (10 d)	CB-IV	(Cheng et al., 2010)
	Tung Chung	Urban	Jan 2005-Dec 2014	Month-to-month (5 months)	CB05	(Whalley et al., 2021b)
Chengdu	Pengzhou	Suburban	3 Sep–2 Oct 2016	Entire period	RACM2	(Tan et al., 2018b)
	Pixian	Suburban				
	Shuangliu	Suburban				
	Chengzhong	Urban				
Zhuhai	Qi'ao	Mountain	25 Sep–28 Oct 2016	Entire period	MCMv3.2	(Liu et al., 2021b)
Wuhan	HPEMC[d]	Urban	Feb 2013-Oct 2014	Month-to-month (21 months)	MCMv3.2	(Lyu et al., 2016)
Guangzhou	GZ	Urban	5–17 Jul 2006	Day-to-day (16 d)	CB-IV	(Lu et al., 2010)
	BZ	Suburban				
	Guangzhou Xinken	Nonurban	4 Oct–5 Nov 2004	Entire period	SAPRC	(Zhang et al., 2008b)
Hangzhou	Zhaohui Xiasha	Urban Suburban	17 May, 26 Jun 20, Jul 24, Aug and 26 Sep	Entire period (5 d)	MCMv3.3.1	(Zhao et al., 2020)

City	Site	Type	Sampling period	Modeling timescale[a]	Mechanism	Reference
	Huapu	Urban				
Nanjing	NUIST[e]	Suburban	3 Jul–1 Aug 2018	Entire period	CB-IV	(Fan et al., 2021)
	SORPES	Suburban	22 Sep–7 Oct 2014	Day-to-day (8 d)	MCMv3.3.1	(Xu et al., 2017)
Yulin	EMB[f]	Urban	7 Jul–10 Aug 2019	Day-to-day (13 d)	MCMv3.3.1	(Yin et al., 2021)
Lanzhou	Renshoushan Park	Urban	19 Jun–16 Jul 2006	Day-to-day (3 d)	MCMv3.2	(Xue et al., 2014)
Baoding	EPB[g]	Urban	10–30 Sep 2015	Day-to-day (5 d)	MCMv3.3.1	(Wang et al., 2020a)
Chongqing	Nan Quan	Suburban	24 Aug–22 Sep 2015	Day-to-day (7 d)	MCMv3.2	(Li et al., 2018)
	Chao Zhan	Urban				
	Jin Yun Shan	Urban				
Shanghai	Pudong	Urban	1–31 Jul 2017	Day-to-day (16 d)	CB-IV	(Lin et al., 2020)
	Dianshanhu	Suburban				
South China Sea	Wanshan Island	Island	11 Sep–21 Nov 2013	Entire period	MCMv3.2	(Wang et al., 2018)

[a]Number of days for modeling the patterns of time scale denotes that which was simulated by the box model.
[b]Peking University
[c]Shenzhen Yanjiusheng Yuan
[d]Hubei Provincial Environmental Monitoring Center
[e]Nanjing University of Information Science & Technology
[f]Environmental Monitoring Building
[g]Environmental Protection Bureau

911   **Table 2.** Summary of the number of days (for model calculation) and proportions that
912   were classified into the three photochemical regimes across each site and multiple
913   patterns of time scale.

Patterns of Time scale	Site	Photochemical regime: RIR_{NOx}/RIR_{AVOC}					
		NO_x-limited: >2		Transition: 0.5~2		VOC-limited: <0.5	
		No. of days	Proportion	No. of days	Proportion	No. of days	Proportion
Month-to-month	TZ	2	40%	2	40%	1	20%
	BJ	0	0%	3	60%	2	40%
	XD	0	0%	2	40%	3	60%
Week-to-week	TZ	7	33%	8	38%	6	29%
	BJ	0	0%	10	50%	10	50%
	XD	3	16%	6	32%	10	53%
Day-to-day	TZ	29	29%	45	45%	26	26%
	BJ	0	0%	21	26%	60	74%
	XD	20	18%	23	20%	71	62%

914

915
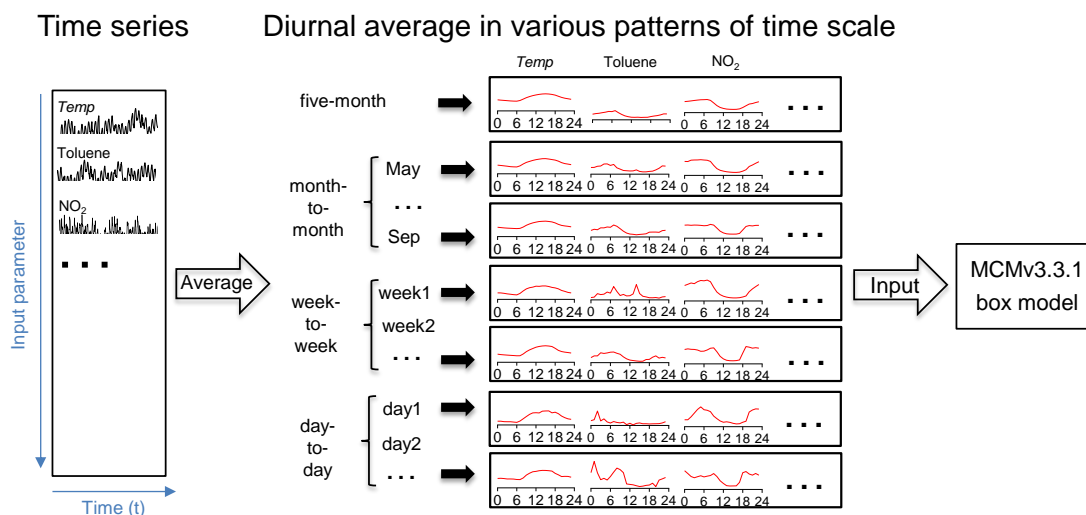
916 **Figure 1.** Schematic diagram of the dataset treatment to derive four patterns of time scale for 0-D box

917 model input. Note that the four patterns (i.e., five-month, monthly, weekly, and daily) were the diurnal

918 average of the initial dataset. This diagram takes one site and several input measurements (temperature,

919 toluene, and NO_2) as examples.
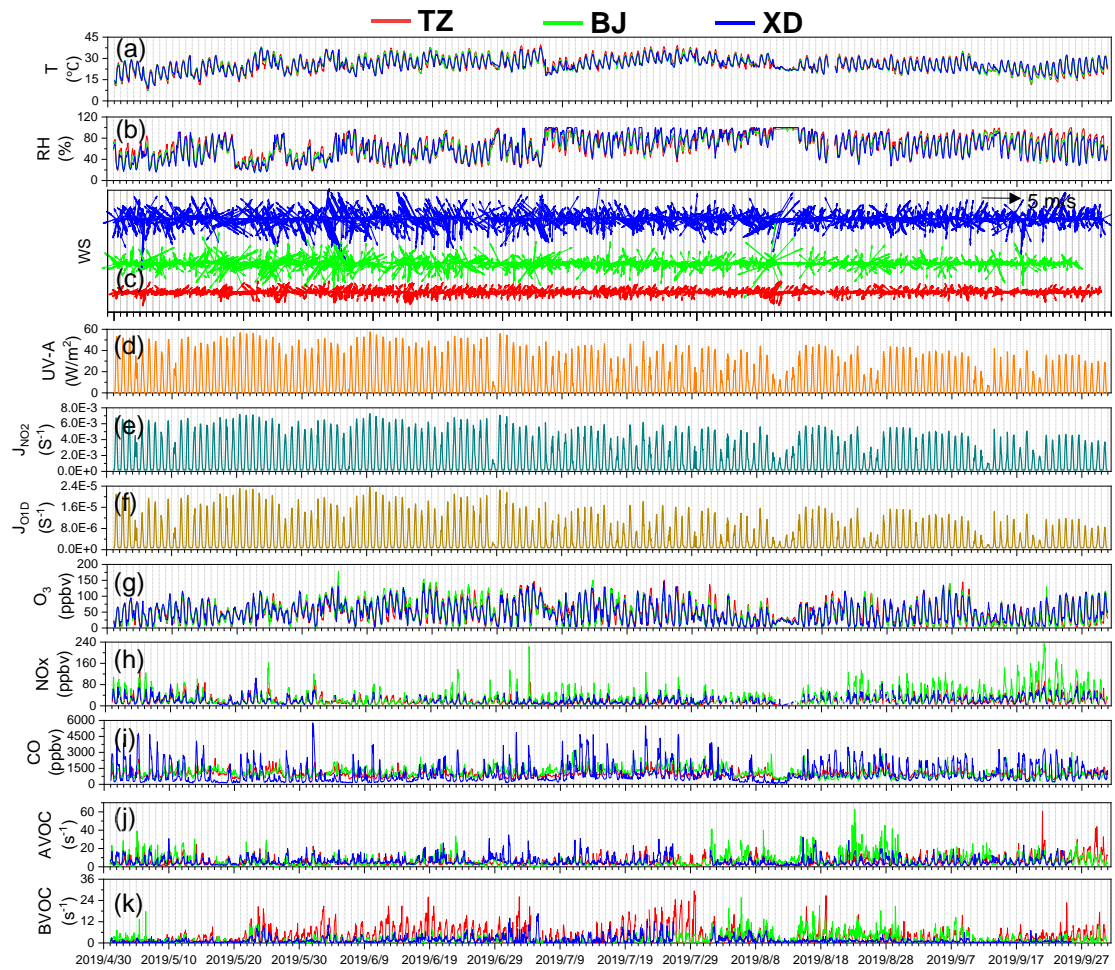
Figure 2. Time series of meteorological parameters, O₃ and its precursors (i.e., CO, NOₓ, VOCs) throughout the whole campaign at the three sites in Zibo.

923

924
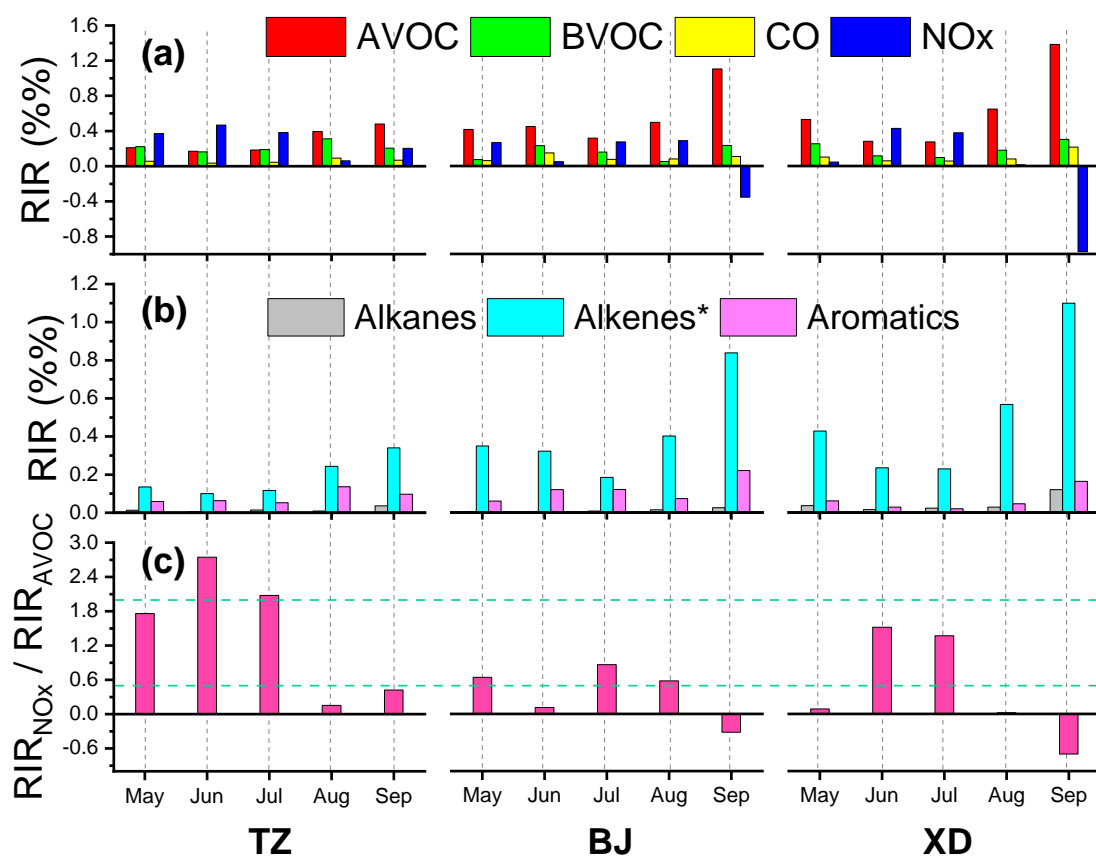
Figure 3. Time series of month-to-month RIR values of major precursor groups and RIR_{NOx}/RIR_{AVOC} at three sites (TZ, BJ and XD) in Zibo. The green dash line indicates to $RIR_{NOx}/RIR_{AVOC} = 0.5$ and 2.

927
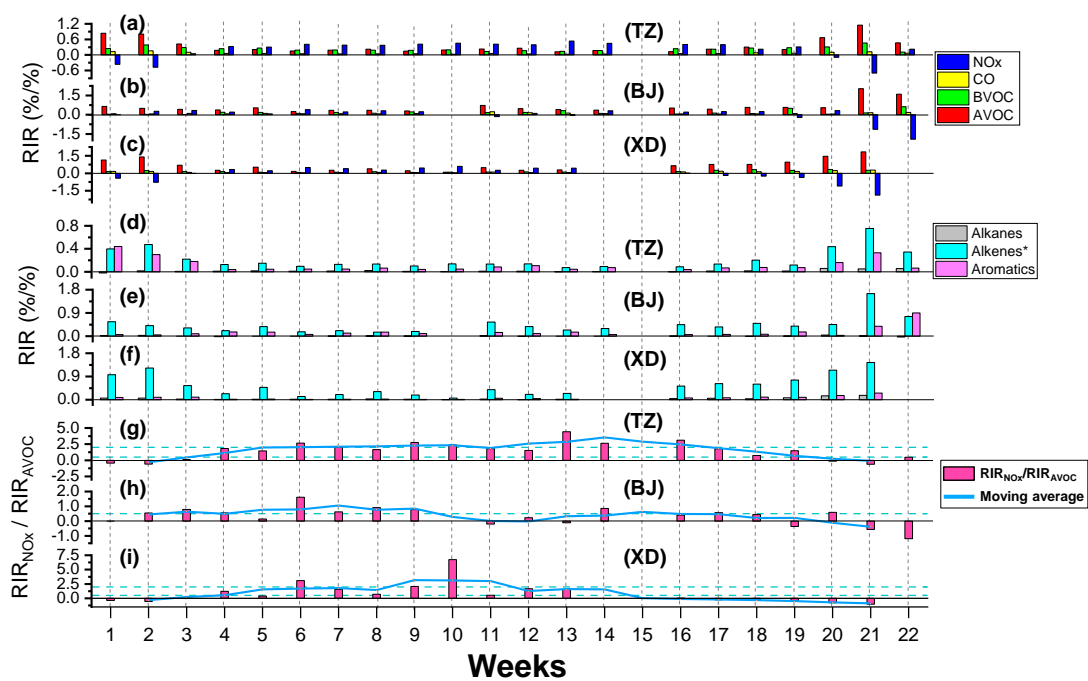
928
929 **Figure 4.** Time series of week-to-week RIR values of major precursor groups and RIR_{NOx}/RIR_{AVOC} at
930 three sites (TZ, BJ, and XD) in Zibo. The blue lines in (g)-(i) are the three points moving average of
931 RIR_{NOx}/RIR_{AVOC} value.
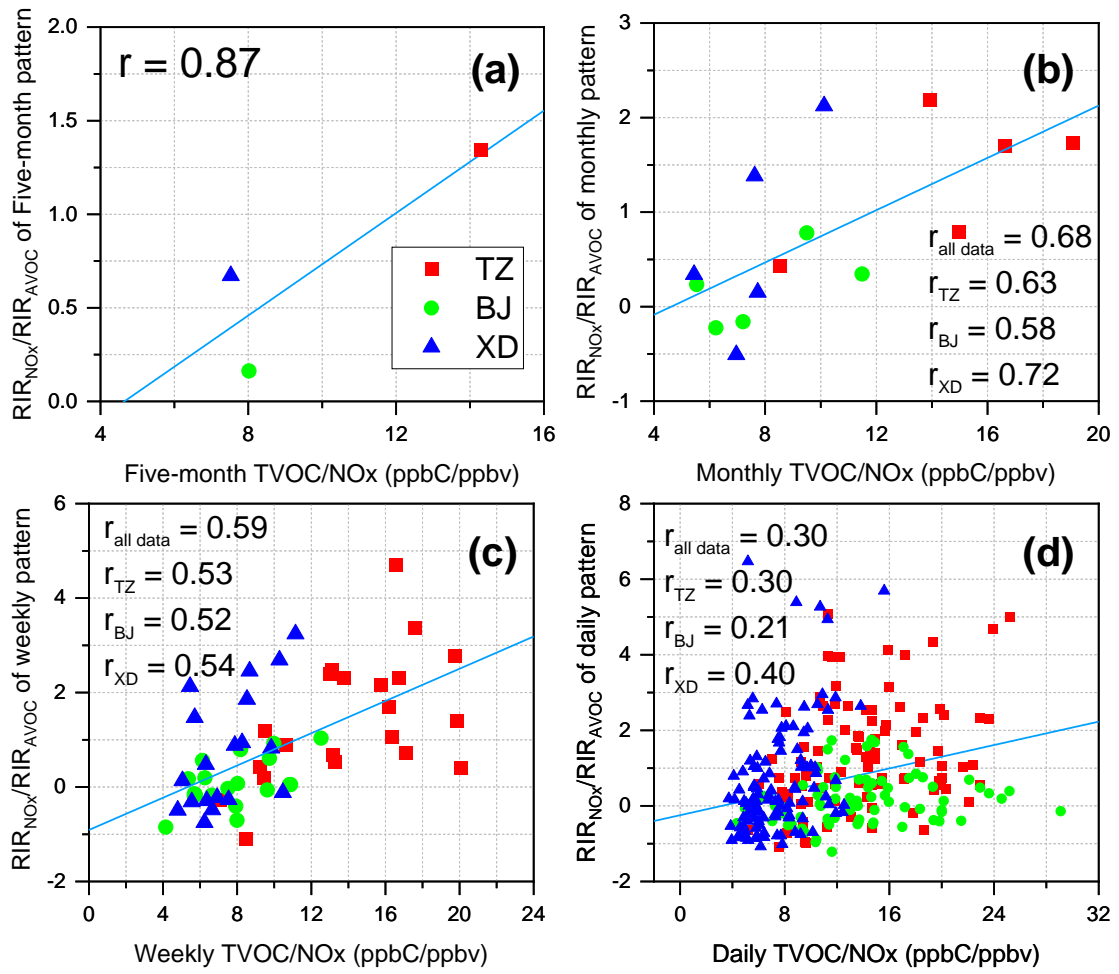
932
933 **Figure 5.** The correlations of TVOC/NO$_x$ with RIR$_{NOx}$/RIR$_{AVOC}$ at multiple patterns of time scale at the
934 three sites in Zibo.

935
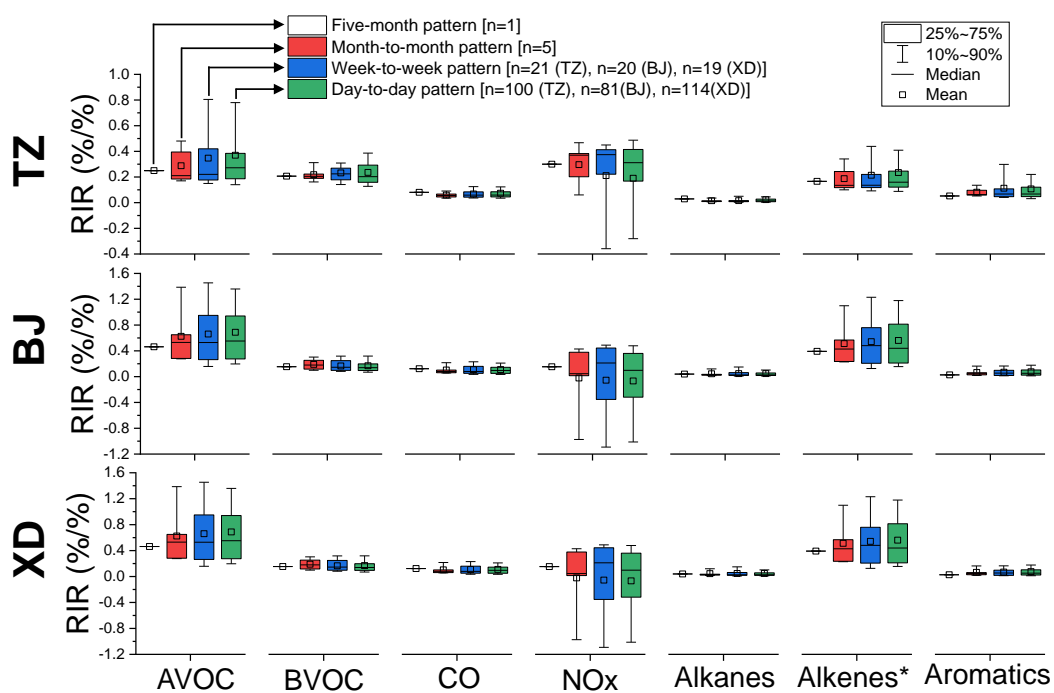
936
937 **Figure 6.** Distribution of RIR values of major precursor groups in multiple patterns of time scale at three
938 sites (TZ, BJ, and XD) in Zibo.

939

940 **Figure 7.** Distribution of RIR$_{NOx}$/RIR$_{AVOC}$ (indicator of photochemical regime) in multiple patterns of
941 time scale at three sites (TZ, BJ, and XD) in Zibo.
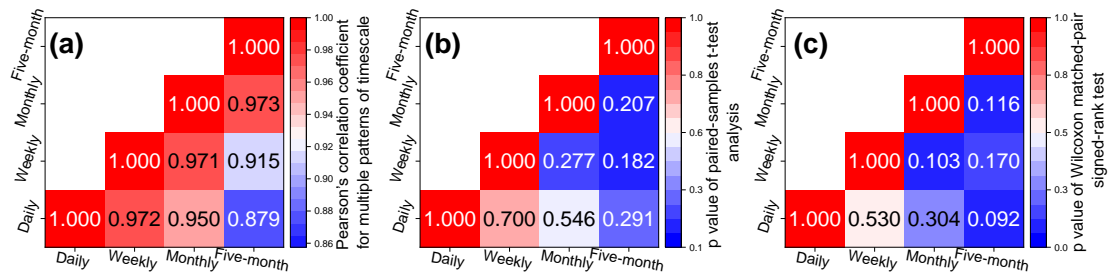
Figure 8. The statistical analysis results of RIR values (from Table S6) at multiple patterns of time scale: (a) Pearson's r correlation analysis (all the results have passed statistical significance assumed at $p < 0.01$), (b) Paired-samples t-test analysis ([*]p values refer to differences with a statistical significance assumes at $p < 0.05$), (c) Wilcoxon matched-pair signed-rank test ([*]p values refer to differences with a statistical significance assumes at $p < 0.05$).
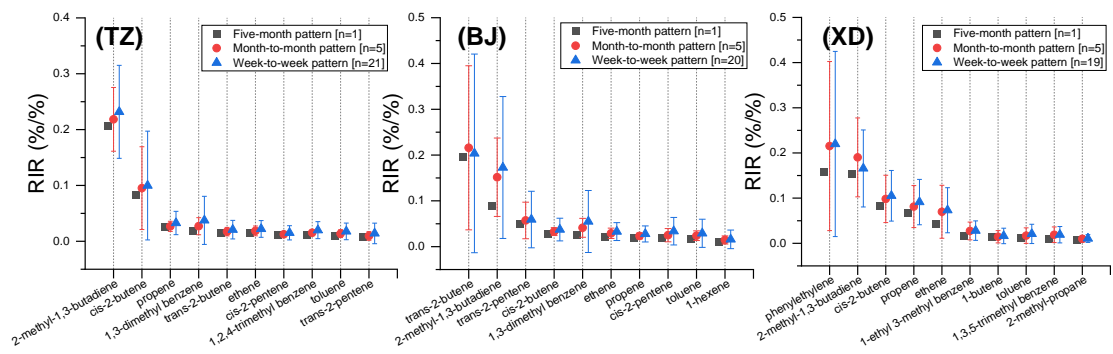
948
949 **Figure 9.** Averaged RIR values of individual AVOC species (top 10) at different patterns of time scale at

950 three sites (TZ, BJ, and XD) in Zibo. The error bars represent the standard deviations of the mean.